

## **CONSTITUTIVE MODELS FOR HARDENING OF TEMPERED MARTENSITIC STEELS IRRADIATED AT 300 TO 500°C UP TO HIGH DPA AND HE - T. Yamamoto, G.R. Odette (University of California Santa Barbara)**

### **OBJECTIVE**

The objective of this work is to develop models of irradiation effects on the constitutive properties of 9Cr tempered martensitic steels, including the effects of He and nanoscale precipitation at high dpa.

### **SUMMARY**

We update irradiation hardening models for 9Cr tempered martensitic steels (TMS), based largely on the UCSB database, which currently contains 2334 tensile and 353 hardness data and 382 microstructural data points. This database mainly includes results from neutron (NI) and spallation proton (SPI) irradiations. The expanded database is used to fit phenomenological models of yield stress changes ( $\Delta\sigma_y$ ) as a function of the NI and SPI dose (in displacement-per-atom, dpa), irradiation ( $T_i$ ), test temperatures ( $T_t$ ) and He concentration (He). Notable advances include: a) update of predictive dpa damage dominated  $\Delta\sigma_y(\text{dpa}, T_i, T_t)$  models, including demonstration and quantification that 9Cr TMS continue to harden, after an intermediate dpa plateau, at rates that are likely linked to minor alloy solute contents; this is likely in association with increasing segregation driven nanoscale precipitation of MnNiSi phases on dislocations; b) refinement of high  $T_i$  softening rates in dpa dominated irradiations; c) quantification of high He contributions to hardening, above an  $\approx 500$  appm threshold, as a function of a wide range of  $T_i$ , dpa and He (appm/dpa); d) quantification of the effect of high He on the post yield flow stress ( $\sigma_{fl}$ ) in reducing the irradiation induced loss of strain hardening; e) refinement of the He bubble hardening factor ( $\alpha_b$ ) and comparison of  $\alpha_b$  to atomistic models; e) dispersed barrier modeling of in situ helium injection microstructure hardening, including high He effects on enhancing loops and loop strengthening factors, which, along with bubble contributions, result in predictions that are consistent with observed  $\Delta\sigma_y$ .

### **PROGRESS AND STATUS**

#### **Introduction**

An important objective for the fusion materials research is to develop quantitatively predictive models for irradiation induced changes in 9Cr TMS constitutive properties as a function of the *combination* of all significant metallurgical and irradiation variables. The metallurgical variables include the start-of-life alloy composition, microchemistry and microstructure, including the effects of product form (weld and base metal) and thermo-mechanical processing treatment (TMT) history. The primary irradiation variables include irradiation temperature ( $T_i$ ), stress and the total and rates of production of damaging species, including for displacements-per-atom (dpa), helium (He), hydrogen (H) and a range of solid transmutation products (appm). Post-irradiation testing and data analysis variables are also significant. For example,  $\Delta\sigma_y$  depends on the test temperature ( $T_t$ ) and strain rate ( $\dot{\epsilon}$ ) [1,2]. Ultimately linked multiscale models will sequentially relate: a) the primary variables to microstructural evolutions; b) the effects of these evolutions on fundamental structure-sensitive constitutive and local fracture properties; c) and the consequences of changes in these fundamental properties to more complex engineering properties, like shifts in fracture toughness Master Curve reference temperatures,  $\Delta T_o$ , or corresponding Charpy shifts,  $\Delta T_c$ . [1,2]. We have continued to accumulate tensile and other mechanical property as well as microstructure data, with a special emphasis of the hardening and embrittlement effects of high concentration of He that persists

even at high temperature. High He also reduces the loss of strain hardening generally observed in neutron-only (dpa dominated) irradiated TMS [3]. This is significant since, for example, engineering tensile ductility is enhanced and changes in the average flow stress between 0 to 10% plastic strain are more directly correlated to hardening induced  $\Delta T$  than  $\Delta\sigma_y$  [4]. Thus, true stress-strain curves are also analyzed to quantify He effects on  $\Delta\sigma_{fl}$ . Another focus is the re-initiation of hardening, following an intermediate dpa plateau, that is now being observed at higher dpa, likely in association with the nm-scale MnNiSi precipitates (MNSP) that form and grow on dislocations.

### Approach to developing hardening $\Delta\sigma_y(\text{dpa}, \text{He}, T_i, T_t, \text{material})$ models

The low He dominated  $\Delta\sigma_y$ -dpa trends are separated by irradiation type and temperature. The alloys are divided into four broad categories: a) F82H; b) Eurofer97; c) other 9CrW steels containing 1-2%W; and d) 9CrMo steels containing 0.5 to 1.5%Mo. The following approach was taken to derive the hardening models:

1) The displacement damage (dpa) induced hardening models,  $\Delta\sigma_{yn}(\text{dpa}, T_i, T_t, \text{material})$ , were refit to the updated NI (low He) data for the various alloy subsets, distinguished by the alloy class, as well as the irradiation and test temperatures  $T_i$  and  $T_t$ . The new model is a combination of simple saturating Makin and Minter model [5,6] and a Mn-Ni-Si precipitation (MNSP) hardening model at high dose as:

$$\Delta\sigma_{yn} = \Delta\sigma_{ys} [1 - \exp(-\text{dpa}/\text{dpa}_o)]^{1/2} + C_{yp} (\sqrt{\text{dpa}} - \sqrt{\text{dpa}_p}) \quad (1)$$

Here  $\Delta\sigma_{ys}$  is initial saturation hardening,  $\text{dpa}_o$  is the dpa to reach 80% of  $\Delta\sigma_{ys}$ ,  $C_{yp}$  is precipitate hardening coefficient (MPa/ $\sqrt{\text{dpa}}$ ) in the  $\sqrt{\text{dpa}}$  dependent term, and  $\text{dpa}_p$  is the onset dose for precipitation hardening. Simpler form without the MNSP term or simple linear  $C\sqrt{\text{dpa}}$  type fits were adopted in some cases that were indicated by the data, like at high  $T_i$ , or with limited number of data points at lower dpa. Figure 1 shows an example of  $\Delta\sigma_y$  versus  $\sqrt{\text{dpa}}$  for NI of Eurofer97 irradiated at  $\approx 300^\circ\text{C}$  up to  $\approx 80$  dpa. There, stages of  $\Delta\sigma_y(\text{dpa})$  are observed: an initial rapid increase up to a plateau; b) an intermediate dpa  $\Delta\sigma_y$  plateau; and, c) re-initiation of linear increase of  $\Delta\sigma_y$  with dpa above  $\approx 16$  dpa.

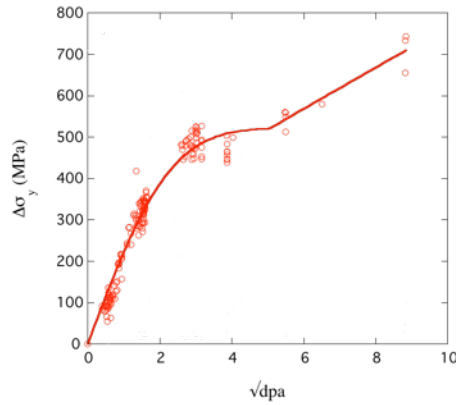


Figure 1 An example of  $\Delta\sigma_y$  versus  $\sqrt{\text{dpa}}$  for NI of Eurofer97 irradiated at  $\approx 300^\circ\text{C}$  up to  $\approx 80$  dpa for room temperature (RT) tests.

2) The effect of high He was estimated from the SPI data,  $\Delta\sigma_y(\text{dpa}, \text{He}, T_i, T_t, \text{material})$ , by simply decomposing the dpa induced and He induced dispersed barrier hardenings,  $\sigma_n$  and  $\sigma_{He}$ , as:

$$\Delta\sigma_y(\text{dpa}, \text{He}, T_i, T_t, \text{material}) = S (\sqrt{\sigma_n^2 + \sigma_{He}^2}) + (1-S)(\sqrt{\sigma_n^2 + \sigma_{He}^2 + \sigma_U^2} - \sigma_U) \quad (2)$$

Here, S controls mixture of linear-sum (LS) and root-sum-squares (RSS) super-positioning as described in more details below,  $\sigma_U$  is pre-existing feature hardening of  $\approx 203\text{MPa}$ .  $S = 0.2$ , typically found in microstructure based hardening models also described below is used for simplicity.

3)  $\sigma_{He}(He, \dots)$  is estimated as the difference between SPI and NI data points for a range of He and  $T_i \approx T_t$ .

4) dpa induced  $\Delta\sigma_y(dpa, T_i, T_t, \text{material})$  and He hardening  $\sigma_{He}(He, \dots)$  models are super imposed to constitute a model  $\Delta\sigma_y(dpa, He, T_i, T_t, \text{material})$  describing hardening for various dpa and He conditions.

### He effects on flow stress hardening $\Delta\sigma_{fl}$

The flow stress  $\sigma_{fl}$  is taken as the average of the true stress – strain,  $\sigma(\epsilon)$ , from  $\epsilon = 0$  to 10% plastic strain. Deformation in tensile tests takes place under necking conditions since the uniform elongation for NI steels is typically  $< 1\%$ . We previously developed an iterative finite element (FE) inverse method to derive  $\sigma(\epsilon)$  beyond the necking [3,7]; multiple iterations require a large number of FE runs. Here new simplified method was used to derive  $\sigma_{fl}$ , which works well, at least for 0 to 10%  $\sigma_{fl}$  strain range, as shown by comparisons with cases where the iterative FE was applied previously. Details of the new method will be described in a future report, Here the derived true  $\sigma(\epsilon)$  were used to estimate  $\Delta\sigma_{fl}$  in comparison to  $\Delta\sigma_y$ . It was found that  $\Delta\sigma_{fl}/\Delta\sigma_y$  depends on He.

### Microstructure based hardening models

*Hardening Contributions of Individual Features:* As has been reported previously simple dispersed obstacle individual hardenings were super-positioned appropriately considering the dislocation bowing limits of multiple features, like various precipitates, dislocation loops, bubbles and voids. The individual models for isolated obstacle hardening, based on single dislocation obstacle interactions, can be expressed in various ways but the most frequent and simplest formulation is [8.9]

$$\sigma_j = M\alpha_j(r_j)Gb/(L - 2r_j) \quad (3a)$$

Here, the spacing between the centers of the obstacles is

$$L \approx 1/\sqrt{(2N_j r_j)} \quad (3b)$$

Here  $N_j$  and  $r_j$  are the feature number density and radius, respectively. The  $\alpha_j$  is the obstacle-dislocation interaction strength parameter,  $M \approx 3.06$  term is the polycrystalline Taylor factor for bcc lattices,  $G$  is the shear modulus ( $\approx 82000\text{ MPa}$  at  $25^\circ\text{C}$ ) and  $b = 0.248\text{ nm}$  is the dislocation Burgers vector. Here we focus on refining the bubble  $\alpha_b$ .

*Strength Superposition Models:* Earlier computer simulations showed that the net  $\Delta\sigma_y$  based on the individual yield stress contributions from combinations of weak ( $\alpha_w < 0.05$ ,  $\sigma_w$ ), medium ( $0.05 < \alpha_m < 0.6$ ,  $\sigma_m$ ) and high ( $\alpha_s > 0.6$ ,  $\sigma_s$ ) strength obstacles can be described by a simple fitted analytical expression interpolating between root sum square (RSS) and linear sum (LS) rules [7]:

$$\Delta\sigma_y = \sigma_w + (1-S)(\sigma_m^2 + \sigma_s^2)^{1/2} + S(\sigma_m + \sigma_s) - \sigma_s \quad (4)$$

Here the superposition factor  $S$  is [9-11]

$$S \approx \alpha_{so} - \alpha_{m0} (5.0 - 3.3\alpha_{so}) \quad (5)$$

Here the  $\alpha_{io}$  are for an isolate single obstacle based on the critical angle when dislocations bypass the obstacle. The strength factors  $\alpha_i$  used in Equation 1 are for randomly distributed obstacles, which is

related to  $\alpha_{i0}$  by [6,12],

$$\alpha_i = \alpha_{i0}^{3/2} \quad (\alpha_{i0} < 0.64) \quad \text{or} \quad 0.8 \alpha_{i0} \quad (\alpha_{i0} \geq 0.64) \quad (6)$$

Thus, obstacles with similar strengths can approximately be described by an RSS superposition model, while those with very different strengths (very low and high) come closer to a LS law. The superposition of the strengthening contributions of medium strength and strong obstacles falls in between.

The model has been calibrated to neutron irradiated Fe-Cr alloys and TMS, to determine the  $\alpha_j$ , for dislocation loops (DL), solute clusters and G-phase precipitates (SC and P),  $\alpha'$  Cr-rich phases and pre-existing strong obstacles ( $\text{Mo}_2\text{C}$  and network forest dislocations), as shown in Table 1. G-phase like MnNiSi precipitates hardening is based on Russel-Brown model calibrated by database for reactor pressure vessel (RPV) steels. The models were also calibrated to hardening in SPI and post-irradiation annealed (PIA) SPI microstructures to determine the  $\alpha_b$  for He bubbles and small defect clusters. Here, refined  $\alpha_b$  were used to model  $\Delta\sigma_y$  from the observed microstructure formed by in-situ He injected (ISHI) at high  $T_i$ , where NI (low He) would lead softening.

Table 1. Previously determined  $\alpha_j$  values and pre-existing obstacle hardening ( $\sigma_u$ )

Obstacle	Strength, $\alpha_j$	Value
Dislocation loop	$\alpha_{DL}$	0.224
Small solute cluster	$\alpha_{SC}$	0.224
$\alpha'$ precipitate	$\alpha_{\alpha'}$	0.040
G-phase precipitate	$\alpha_p$	$\approx 0.26$
Pre-existing (like from $\text{Mo}_2\text{C}$ )	$\alpha_u$	0.8
	$\sigma_u$	203 MPa

The calculated ISHI  $\Delta\sigma_y$  was used to help estimate the  $T_i$  dependence of He contributions to hardening. The  $\alpha_b$  was compared to values independently reported elsewhere, and to the predictions of MD atomistic models.

## Results

### Hardening models for dpa dominated neutron irradiation data

Figure 2 summarizes the neutron dpa induced  $\Delta\sigma_{y,N}$  versus  $\sqrt{\text{dpa}}$  trends for the material groups: a) F82H; b) Eurofer 97; c) 9Cr-1-2W steels; d) 9Cr-1Mo steels; and temperature bins 1)  $T_i < 225^\circ\text{C}$ ; 2)  $250 \pm 25^\circ\text{C}$ ; 3)  $310 \pm 35^\circ\text{C}$ ; 4)  $360 \pm 15^\circ\text{C}$ ; 5)  $400 \pm 25^\circ\text{C}$ ; 6)  $450 \pm 25^\circ\text{C}$ ; 7)  $500 \pm 25^\circ\text{C}$ ; and 8)  $> 525^\circ\text{C}$ . Fitting to Eq.(1) was carried out when the data subset is large enough to derive a pertinent saturating trend. A simple linear fit was used for high temperature cases where softening takes place, and saturation behavior is not observed.

The  $T_i = 310 \pm 35^\circ\text{C}$  F82H and Eurofer 97 result in good fits to the saturating-rehardening trend is seen in Figure 2. In other cases the  $\Delta\sigma_y$  data are generally fewer and more scattered. Table 2 summarizes the best-fit parameters for the temperature bins for all the alloy groups. The F82H (2a), Eurofer97 (2b) and 9CrW (2c) alloys have a similar saturation  $\Delta\sigma_{ys} \approx 433 \pm 10$  MPa, and is highest in the 9CrMo (2d) alloys. However, the  $dpa_o$  is significantly lower for Eurofer 97 (the initial hardening rate is faster). The MNSP hardening is larger in Eurofer 97 than in F82H, with both a lower  $dpa_p$  and a higher  $\Delta\sigma_{yp}$ -hardening rate. The  $\Delta\sigma_{yp}$ -hardening rate is even higher in the 9Cr2W steels, and highest in the 9CrMo alloys. Typical *nominal* Mn, Ni and Si contents in F82H are 0.12%, 0.02% and 0.1%, while those in Eurofer 97 are 0.5%, 0.02, and 0.05%, respectively. The difference in Mn content is considered to be the main reason for the larger MNSP  $\Delta\sigma_{yp}$  in Eurofer97. The MNSP hardening is even larger in the 9CrW and 9CrMo steels. The key 9CrW alloy contains 0.5% Mn, 0.02% Ni and 0.2% Si, while the 9Cr-1Mo alloys contain more Ni  $\approx 0.2$  and Si  $\approx 0.3$ , leading to the highest  $\Delta\sigma_{yp}$  hardening rate. Note these compositions, in wt.%, are nominal and vary considerably, in the range of several tenths of a percent. More detailed analyses of the MNSP hardening including alloy chemistry dependence will be carried out in the future research.

There are a significant number of F82H  $\Delta\sigma_y$  data points at higher  $T_i$  up to  $\approx 600^\circ\text{C}$ . While highly scattered, the average trend indicates that  $\Delta\sigma_y$  approaches 0, or slightly softens, at  $T_i = 400 \pm 25^\circ\text{C}$ ; and softening is dominant at higher  $T_i$ . While Eurofer 97 has very limited number of data in the other  $T_i$  bins, the  $\Delta\sigma_y$  are generally consistent with those in the F82H and 9CrW steels. The  $\Delta\sigma_y$  trends for all 9CrW steels in Figure 2c shows: a) the initial  $\Delta\sigma_y$  versus  $\sqrt{dpa}$  slope decreases with increasing  $T_i$ ; b) the saturation  $\Delta\sigma_{ys}$  increases with temperature at low  $T_i$ , peaks at  $T_i = 310 \pm 35^\circ\text{C}$  bin, then decreases, transitioning to softening around  $T_i = 450 \pm 25^\circ\text{C}$ . Trends in 9CrMo steels in Figure 2d also show that the systematic  $T_i$  dependence is similar to that in 9CrW steels, including a hardening to softening transition around  $T_i = 450 \pm 25^\circ\text{C}$ .

Figure 3 shows guide lines summarizing the temperature dependence of the model parameters: a)  $\Delta\sigma_{ys}$ ; b)  $dpa_o$ ; c) the  $\Delta\sigma_y$ -hardening slope (initial slope for the saturating curve or the linear fits). The  $T_i$  dependence for  $\Delta\sigma_{ys}$  and  $dpa_o$  were drawn for 9Cr-1-2W and partially for F82H, but the other alloy groups also follow the similar  $T_i$  trends. The  $T_i$  dependence of hardening slope is also general similarity in all the alloy groups, while softening may start at a lower  $T_i$  in F82H and a higher  $T_i$  in 9Cr1Mo as indicted by the  $\Delta\sigma_y$  at  $T_i=400^\circ\text{C}$ . Softening rates ( $\Delta\sigma_{y,N}/\sqrt{dpa}$ ) do not systematically change for  $T$  in individual alloy datasets, but the linear fitting gives the following  $T_i$  dependence:

$$\Delta\sigma_{y,N}/\sqrt{dpa} = 26.18 - 0.0800T_i \text{ (for F82H)} \quad (7a)$$

$$\Delta\sigma_{y,N}/\sqrt{dpa} \approx 18.0 - 0.0525 T_i \text{ (for all alloys combined)} \quad (7b)$$

Table 2  $\Delta\sigma_{y,N}(dpa)$  model parameters for  $310\pm 35^\circ\text{C}$  data sets

Alloy group	$dpa_o$	$\Delta\sigma_{ys}$	$dpa_p$	$\Delta\sigma_{yp}$	Std. dev.
Euroer97	4.5	437.0	10.1	19.4	32.9
F82H	8.1	424.1	25.1	8.5	43.0
All 9CrW	6.8	436.7	12.0	32.4	61.0
9Cr-Mo	7.7	539.8	4.3	38.1	47.1

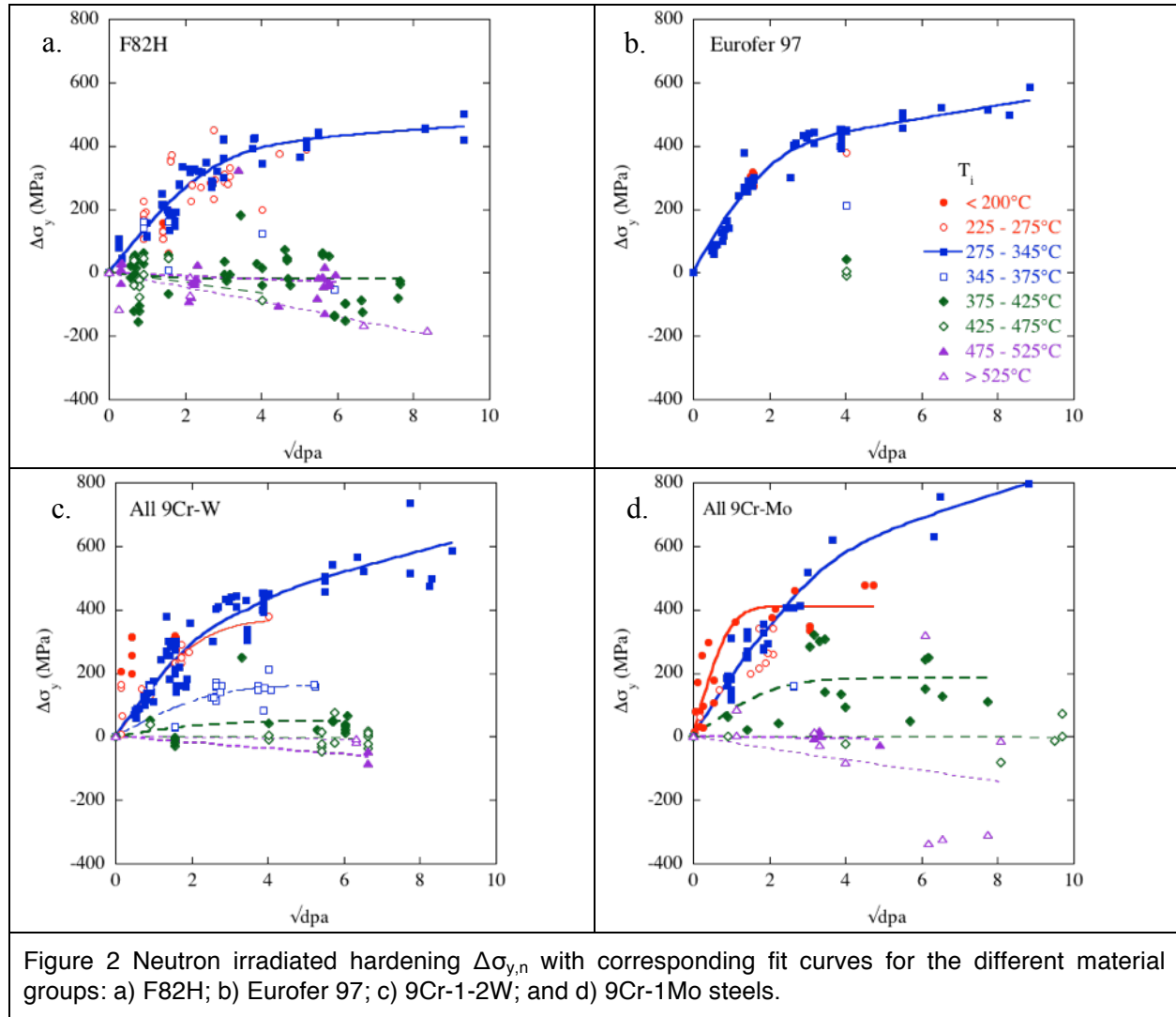


Figure 2 Neutron irradiated hardening  $\Delta\sigma_{y,n}$  with corresponding fit curves for the different material groups: a) F82H; b) Eurofer 97; c) 9Cr-1-2W; and d) 9Cr-1Mo steels.

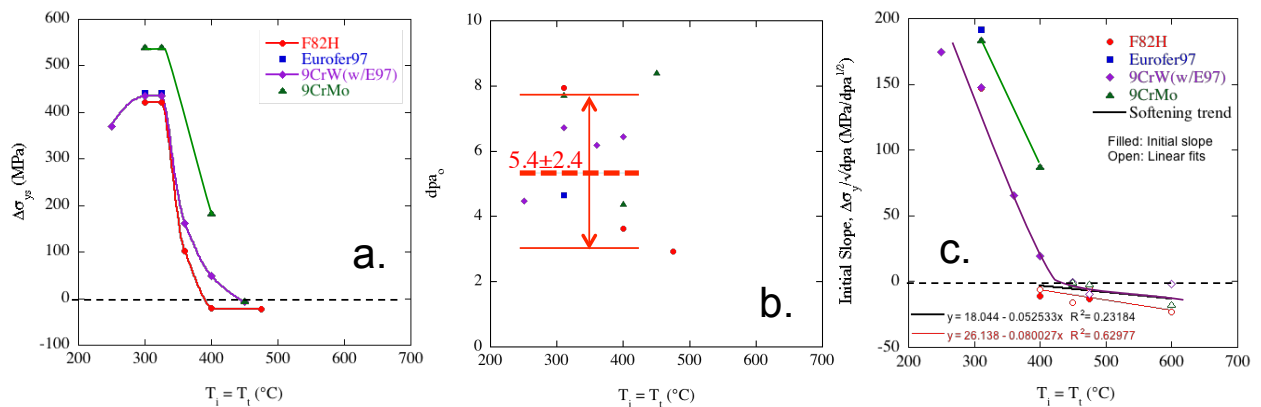


Figure 3 the temperature dependence of  $\Delta\sigma_{y,n}(dpa)$  model parameters: a)  $\Delta\sigma_{ys}$  and b)  $dpa_o$ , as well as c) hardening slope (initial slope for the saturating curve or that of linear fits).

## He contributions to the SPI $\Delta\sigma_y$

Figure 4 shows the isolated He hardening  $\sigma_{He}$  decomposed based on Eq.(2) super-positioning for SPI irradiated F82H and Eurofer97 alloys [13-19] as a function of  $\sqrt{He}$  (appm<sup>1/2</sup>) for  $T_i$  100°C groups. Due to large uncertainties and lack of relevance, the data for  $T_i < \approx 100^\circ\text{C}$  and 9Cr1Mo alloys were excluded. The general softening trends shown in Figure 3c is used for  $\Delta\sigma_{y,N}(\text{dpa}, T_i, T_t)$  for  $T_i = T_t > 450^\circ\text{C}$ . Note, high He SPI  $\Delta\sigma_y$  data are also limited by linear elastic fracture. The elastic tensile fracture data indicate a large reduction of intergranular fracture stress, which will be used in fracture models to be reported in the future. Figure 4 also includes an isolated He hardening decomposed for microstructure observed in ISHI irradiated Eurofer97 at 500°C to 21.2 dpa and 1230 appm He [20]. Obtained  $\sigma_{He} - \sqrt{He}$  trends are similar for F82H and Eurofer97, so the combined trends are that  $\sigma_{He} \approx 0$  at  $He < \approx 433$  appm, then increase  $\approx$  linearly with  $\sqrt{He}$  as:

$$\sigma_{He} = 28.4 (\sqrt{He} - 20.8) \quad (8)$$

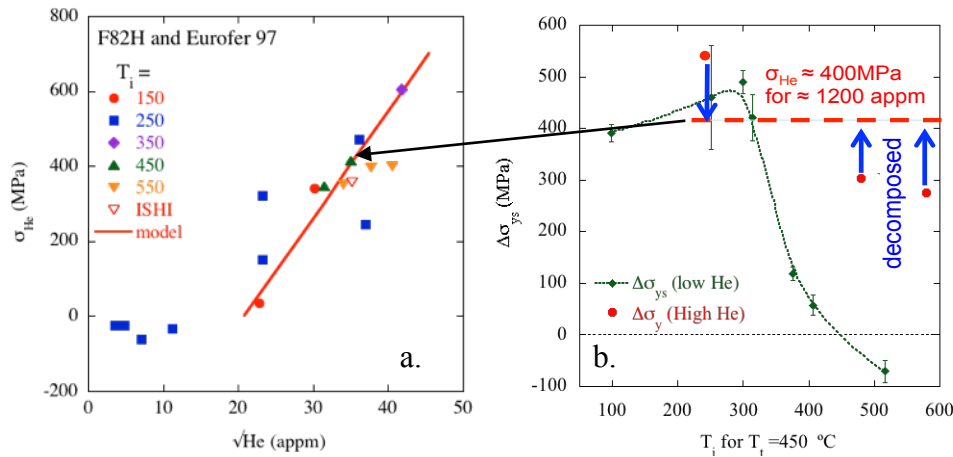


Figure 4 a) Isolated He hardening  $\sigma_{He}$  for SPI irradiated F82H and Eurofer97 alloys shown for  $T_i$  groups with overall fitting for  $He > 500$ . Open triangle is for a hardening estimated for the microstructure observed in ISHI irradiated Eurofer97 at 500°C to 21.2 dpa and 1230 appm He; b) examples of decomposed  $\sigma_{He}$  from SPI  $\Delta\sigma_y$  at various  $T_i$  in relation to low He  $\Delta\sigma_y(T)$  trend.

Combining  $\sigma_{He}(He)$  in Eq(8) with the neutron only  $\Delta\sigma_{y,N}(\text{dpa}, T_i, T_t)$  models can generate  $\Delta\sigma_y$  prediction models for various He/dpa cases. For example, Figure 5 shows a model for F82H at  $He/\text{dpa} = 80$ , corresponding to a typical SPI condition at  $T_i = 300$  to  $500^\circ\text{C}$ . SPI measured  $\Delta\sigma_y$ , plotted along are in good agreement with the models.

## High He effects on flow stress changes

The uniform engineering strains in tensile tests on neutron irradiated TMS (and other metals and alloys) are typically  $< 1\%$ , due to plastic instabilities and immediate necking. However, in SPI steels, with high He, uniform-engineering strains are typically several percent (necking is delayed). Figure 6a shows true stress-strain curves [3,14-15],  $\sigma(\epsilon)$ , used to estimate true flow stress changes. The unirradiated  $\sigma(\epsilon)$  shows typical strain hardening. The NI  $\sigma(\epsilon)$  shows slight initial softening. The  $\sigma(\epsilon)$  with high He concentration do not show immediate drop after yielding suppressing loss of strain hardening, which is generally observed after neutron only irradiation. The effects result in gradual but continuous increase in  $\Delta\sigma_{fl}$  to  $\Delta\sigma_y$  ratio as shown in Figure 6b. This will lead a larger transition temperature shift in fracture toughness, since  $\Delta\sigma_{fl}$  is more directly correlated to  $\Delta T_0$ [4]. It is notable that the total elongation decreases a lot – may be IG fracture occurs after a little strain hardening.

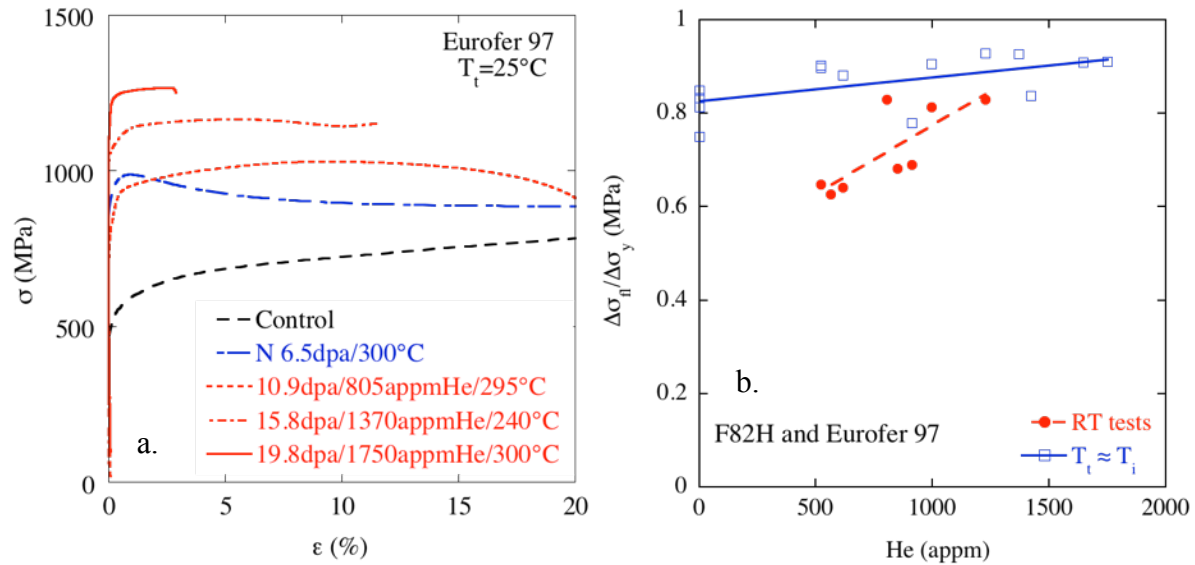
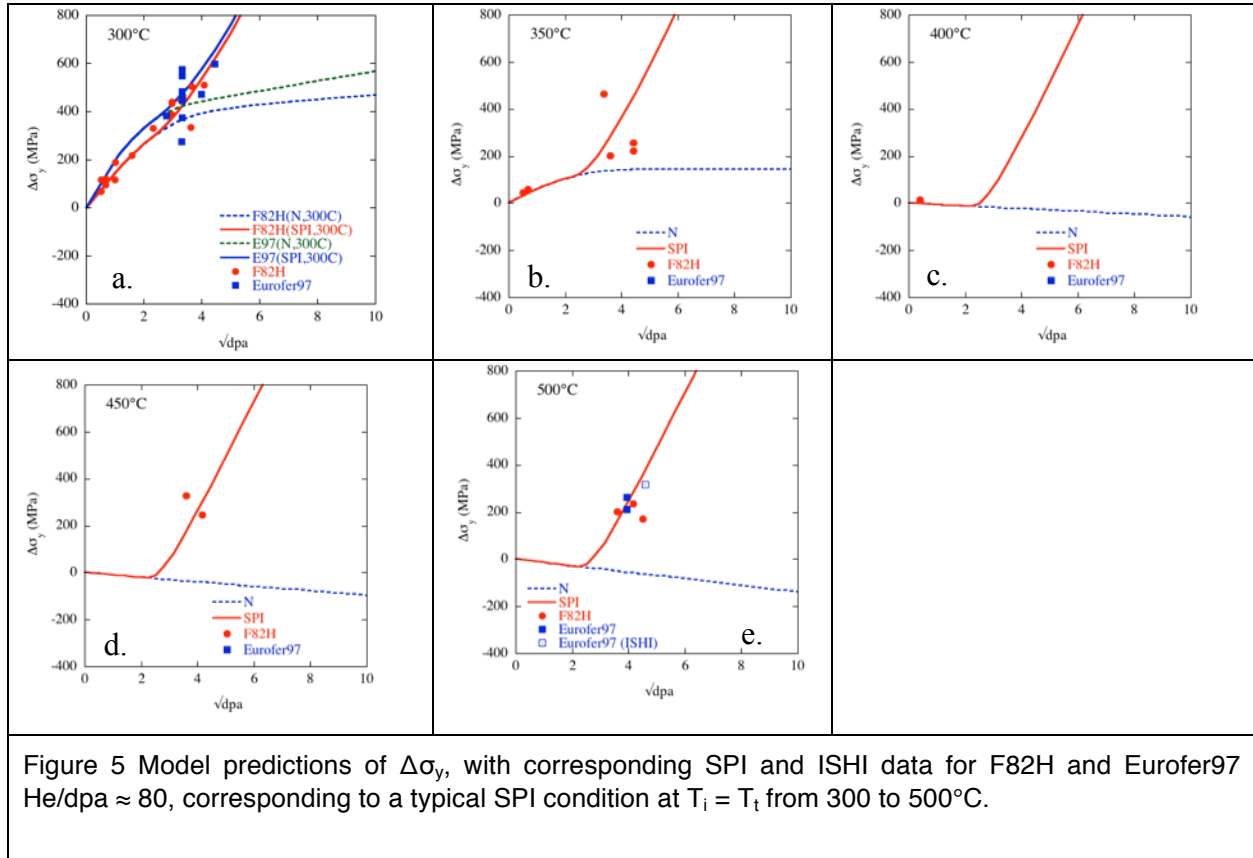


Figure 6 a) True stress-strain curves of Eurofer 97 after various neutron or SPI irradiations; b) the average 0 to 10% strain flow stress change ( $\Delta\sigma_{fl}$ ) to  $\Delta\sigma_y$  change ratio as a function of the He concentration.



## Microstructure-Hardening Model

Our database includes 31 cases where hardening measurements (by hardness or tensile tests) are accompanied by fairly comprehensive microstructural data sets; 15 cases are for post-STIP irradiation annealed microstructure, where only He bubbles are observed. Figure 7 shows the corresponding derived bubble obstacle strength,  $\alpha_b$ , compared to the values reported by Pen, Vieh and others [19,21-23]. The PSI  $\alpha_b$  are, on average, 27% lower than ours. This is due to different assumptions about strength superposition. The PSI analysis did not consider pre-existing hardening features for the annealed bubble only case and used a RSS superposition law in the case of multiple hardening features. In contrast, we used to mixed LS and RSS superposition procedure, accounting for  $\approx 200$  MPa of pre-existing obstacle hardening. Figure 7b shows  $\alpha_b$  as a function of the bubble size compared to the predictions of MD simulations by Osetsky et al. [24]. The MD results for isolated bubbles were converted to randomly distributed bubbles using weak obstacle theory of  $\alpha_b^{3/2}$  [12]. Our results are a factor of 1.29 higher than the MD based values, assuming the Osetsky  $r_b$ -dependence, while the PSI results are lower by factor of 0.87. The heavy dashed curves are simple linear fits of  $\alpha_b$  over the range of  $r_b$ . Given various sources of uncertainty in the data, analysis and model, these results are remarkably consistent, hence, an average  $\alpha_b \approx 0.19$  is appropriate for in modeling He bubble contributions to  $\Delta\sigma_y$ .

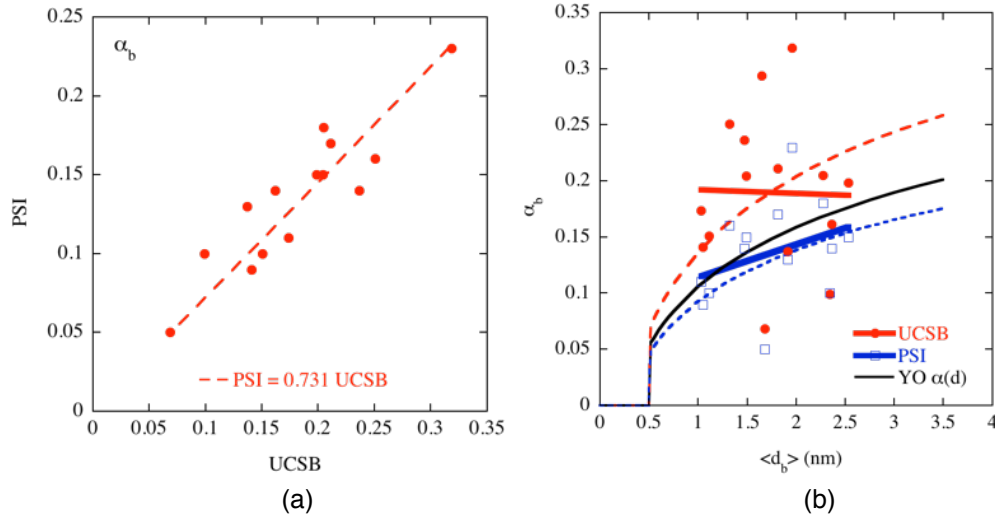


Figure 7 a) Comparisons of UCSB versus PSI estimates of bubble obstacle strength factors ( $\alpha_b$ ) for individual post-SPI annealed (PSA) conditions, with only bubbles in the microstructure; and, b) Osetsky's MD predictions  $\alpha_b$  as a function of the bubble diameter [21] compared to the UCSB and PSI evaluations along with heavy fitted lines. Note the Figure 7b has one more UCSB data point than in 7a.

The size dependent and average  $\alpha_b$  were applied to the larger dataset, including as-irradiated conditions, with defect clusters (small solute segregated loops) as well as bubbles. Fitting size-independent single values of  $\alpha_b$  and  $\alpha_{dc}$  resulted in better statistics than using the  $\alpha_b(r_b)$  normalized Osetsky relation determined above. The best fit defects cluster  $\alpha_{dc} \approx 0.328$  and bubble  $\alpha_b \approx 0.17$ , only slightly lower than the average of 0.19 in the case of PIA conditions only. In the case of microstructures with dislocation loops,  $\alpha_{dc}$  and  $\alpha_b$  were found to be 0.354 and 0.165, respectively, with a fixed loop  $\alpha_l = 0.22$ , as previously derived from NI (low He) data. A fitted  $\alpha_l$  increases to an arbitrary limit of 0.5, for fixed  $\alpha_b$  and  $\alpha_{dc}$  of 0.17 and 0.35, respectively. The reason for such a large  $\alpha_l$  is not clear, but may be associated with a loop bubble complex, which are often observed, that they are a stronger obstacle than either bubbles or loops alone. Bubble-loop complex mechanical stability may also be signaled strain hardening versus strain softening behavior with and without high He as described above. These results are summarized in Table 3.

Table 3 Summary of strength factor  $\alpha_i$  used/determined for various datasets

Strength, $\alpha$			S.D. MPa	Datasets used			Methods
Bubble, $\alpha_b$	Defect cluster, $\alpha_{dc}$	Disl. Loop, $\alpha_l$		PIA	As-irrad. (no DL)	As-irrad. (w/ DL)	
0.19 (avg.)	N/A	N/A	n/a	X			$\alpha_b$ derived from individual $\Delta H$ - microstructure pairs
0.17	0.33	N/A	127	X	X		fitted $\alpha_b$ and $\alpha_{dc}$
0.17	0.35	0.22	192	X	X	X	$\alpha_b$ , $\alpha_{dc}$ fitted with $\alpha_l$ fixed.
0.17	0.35	0.5	163	X	X	X	$\alpha_b$ , $\alpha_{dc}$ , $\alpha_l$ ( < 0.5) fitted

A comprehensive microstructural dataset on bubbles, voids and dislocation loops was obtained from an ISHI irradiation carried out in HFIR to 21 dpa and 1230 appm He at 500°C [20]. The ISHI method injects a uniform concentration of He to a depth of  $\approx 6 \mu\text{m}$ . Thus the effects of He can be determined by comparing the microstructures in the implanted and unimplanted (NI only) regions. Thus the  $\alpha_i$  for the various features can be used in dispersed barrier hardening models described above to calculate  $\Delta\sigma_y$ . Table 4 summarizes the ISHI data and model predictions for cold worked F82H and Eurofer97. In the most relevant case of Eurofer97 the model predicts 318 MPa hardening, 284MPa more than neutron only case of 34 MPa. As shown in Figure 4a and 5e, this is remarkably consistent with the SPI data and the value predicted by Equation 8.

Table 4 Summary of the microstructure and predicted hardening in F82H-M3 (20%CW) and Eurofer 97 after ISHI and NI in HIFR.

Alloy	Irradiation				Predicted $\Delta\sigma_y$ MPa	Dislocation loop		Void		Bubble	
	Type	Ti °C	Dose dpa	He appm		<d> nm	N $10^{21}\text{m}^{-3}$	<d> nm	N $10^{21}\text{m}^{-3}$	<d> nm	N $10^{21}\text{m}^{-3}$
F82H M3 (20% CW)	NI	500	21.2		45.9	10.2	2.4			1.3	21.0
	ISHI	500	21.2	1230	459.1	35.0	7.6			2.7	110
Eurofer97	NI	500	21.2		34.3	9.6	2.4				
	ISHI	500	21.2	1230	318.0	28.0	3.9	6.9	7.5	1.8	2.0

### Hardening model predictions for fusion reactor environment

Equation 8 and neutron induced hardening models were combined to predict  $\Delta\sigma_y(\text{dpa}, \text{He}, T_i, T_t)$  for fusion reactor relevant He/dpa = 10 conditions at temperatures from 300 to 500°C by 50°C step as shown in Figure 8 for  $T_i = T_t$ . Dashed curves are for neutron only cases while solid curves are for fusion conditions.

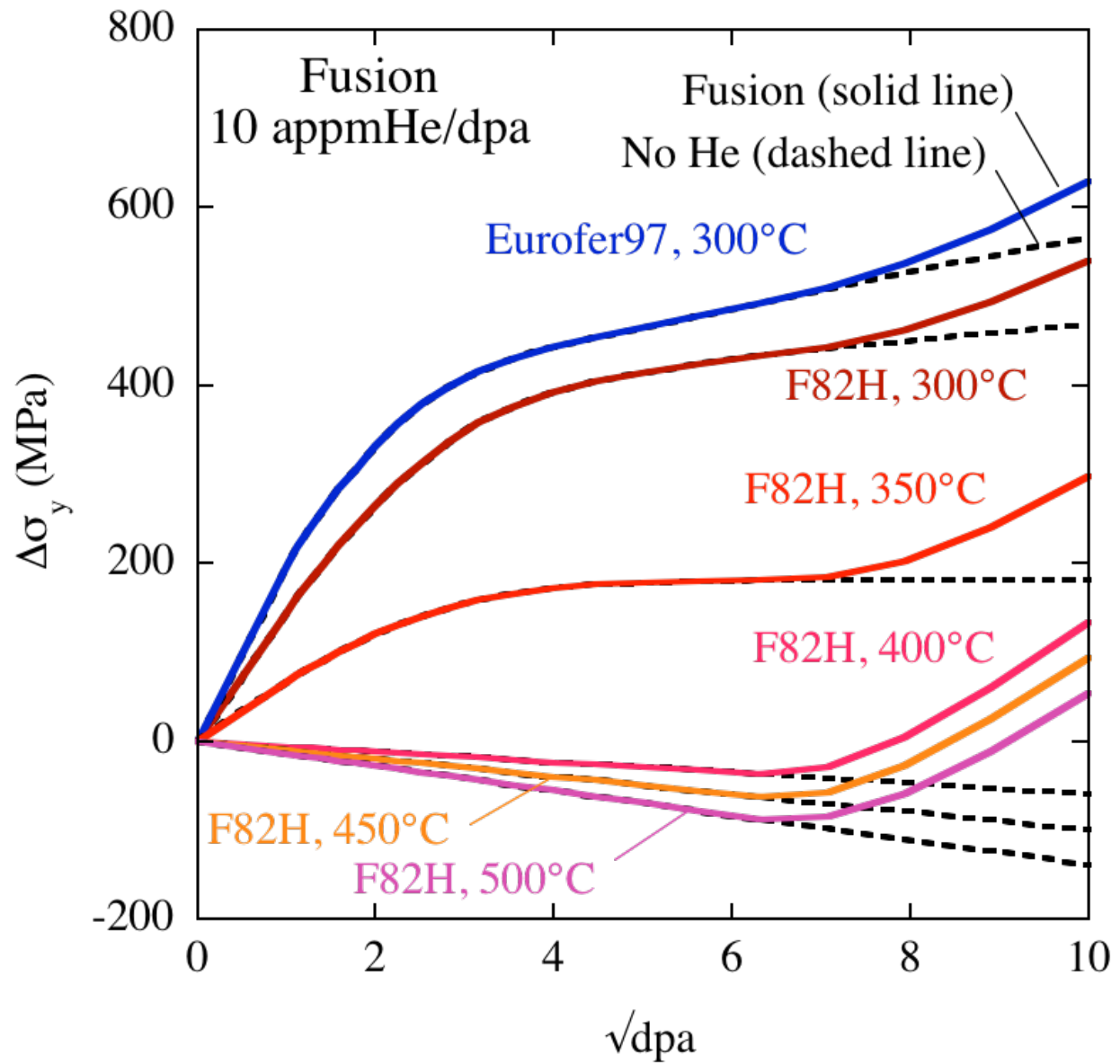


Figure 8 Hardening model  $\Delta\sigma_y$  predictions for F82H at fusion reactor relevant He/dpa = 10 condition for  $T_i = T_t$  from 300 to 500°C. The solid curves are for fusion relevant 10 appm He/dpa, while the dashed curves are for neutron only (He/dpa ≈ 0) conditions.

### Summary and Future Research

We have developed a new toolbox to predict the effects of fission and fusion neutron irradiations on the constitutive properties of 9CrW TMS. The toolbox predicts changes in both yield ( $\Delta\sigma_y$ ) and flow ( $\Delta\sigma_{fl}$ ) stress as a function of dpa, He/dpa,  $T_i$  and  $T_t$ . While not amenable to being described by simple trend curve equations, the model is conveniently coded in an Excel spreadsheet. The model is based on analysis of a large database on mechanical property changes in NI and SPI. It is shown to be in good agreement with the SPI database on high He effects, that was used to quantify the He hardening

contributions. This hardening contribution is fairly independent of  $T_i$ , with a threshold at about 400-500 appm, and subsequently scales with the  $\sqrt{\text{He}}$ . The mechanical property data analysis was complemented by a calibrated microstructure property model applied to a ISHI irradiation experiment; the microstructure based prediction of  $\Delta\sigma_y$  is in excellent agreement with the SPI data trends. The model shows that hardening contributions from He are dominated by enhanced dislocation loop formation, with smaller increases from bubbles. The calibrated model, including all of the hardening contributions, was applied to fusion relevant 10 appm He/dpa  $\approx$  10 conditions for F82H (and Eurofer97 at 300°C).

The database also reveals that high He suppresses loss of strain hardening and low uniform strains, typical of NI conditions. The analysis of NI data also reveals hardening that increases at high dpa due to MNSPs, associated with solute segregation to dislocations. The MNSP hardening varies with the steels impurity/trace element Mn, Ni, Si, P contents. The NI irradiation database also shows that at high temperature the 9CrW steels soften under irradiation, starting at  $T_i$  as low as 450°C, and increasing with dpa. Any significant softening would have enormous structural integrity implications and could severely limit the upper temperature limit for the use of the 9CrW TMS in irradiation service. For example, even modest reductions on strength would have a very larger effect on creep stress allowables [25]

It is important to acknowledge that the database is highly scattered and the various trends that we extracted are not statistically rigorous. The models are also uncertain due to a number of both known and unknown, and unmodeled/untreated physics (such as dislocation loop obstacle strength in He rich environments). However, further discussion of these complex issues will require additional modeling and experimental research. For example, nanoindentation measurements of hardening in the ISHI specimens would be very useful.

Another focus of future research will be to combine the constitutive model presented here, with a treatment of grain boundary weakening by He leading to intergranular fracture in a fracture toughness embrittlement model accounting for the severe synergistic effects of high He [26].

## Acknowledgements

The authors explicitly acknowledge the extensive research that produced the data analyzed in this report and thank the large number researchers around the world for their sustained contributions to the development of materials for fusion energy. Particular thanks goes to Dr. Michael Reith and his FZK/KIT colleagues for generating the Eurofer97 database. We gratefully acknowledge the support provided by U.S. Department of Energy through the Office of Fusion Energy Sciences (8-442520-22419-3).

## References

- [1] G.R. Odette, T. Yamamoto, H.J. Rathbun, M.Y. He, M.L. Hribernik, J.W. Rensman, *J. Nucl. Mater.* 323 (2003) 313.
- [2] T. Yamamoto, G. R. Odette, H. Kishimoto, J-W. Rensman and P. Miao, *J. Nucl. Mater.* 356 (2006) 27.
- [3] S.A. Maloy, T.A. Saleh, O. Anderoglu, T.J. Romero, G.R. Odette, T. Yamamoto, S. Li, J.I. Cole and R. Fielding, *J. Nucl. Mat.* 468 (2016) 232.
- [4] G. R. Odette, M. Y. He, and T. Yamamoto, *J. Nucl. Mater.* 367 (2007) 561.
- [5] M.J. Makin, A.D. Whapham, F.J. Minter, *Philos. Mag.* 7(74) (1962) 285.
- [6] M.J. Makin, F.J. Minter, *Acta. Metall. Mater.* 8 (10) (1960) 691.
- [7] T. Yamamoto, G. R. Odette, S. Li, S. Maloy, T. Saleh, , DOE/ER-0313/58 (2015) 239-245.
- [8] J. W. Martin, *Micromechanisms in Particle-Hardened Alloys*, Cambridge University Press (1980)
- [9] G. R. Odette, Chapter 2 - Embrittlement Mechanisms and Physical Models Underpinning the TTS Model, in the report E. E. Eason, G. R. Odette, R. K. Nanstad and T. Yamamoto, A Physically

Based Correlation of Irradiation-Induced Transition Temperature Shifts for RPV Steels, Oak Ridge National Laboratory ORNL/TM-2006/530 (2007)

- [10] D. Bhattacharyya, T. Yamamoto, P. Wells, E. Marquis, M. Bachhav, Y. Wu, J. Davis, N. Cunningham, A. Xu, G.R. Odette, *J. Nucl. Mater.* 519 (2019) 274-286.
- [11] T. Yamamoto, G.R. Odette, T. Saleh, S. Maloy, Fusion Materials Semiannu. Prog. Rep. 64, DOE/ER-0313/64 (2018) 13-19.
- [12] Foreman AJE and Makin MJ. "Dislocation Movement Through Random Arrays of Obstacles", Can. J. Phys. 1967;45(2):511–517.
- [13] N.Baulc, R.Schaublin, P.Spatig, and M.Victoria, ASTM STP 1447, p341-351
- [14] Z. Tong and Y. Dai, *J. Nucl. Mater.* 385 (2009) 258
- [15] T. Zhang, C. Vieh, K. Wang, Y. Dai, *J. Nucl. Mater.*, 450 (2014) 48.
- [16] B. Long, Y. Dai, N. Baluc, *J. Nucl. Mater.*, 431 (2012) 85.
- [17] Z. Tong and Y. Dai, *J. Nucl. Mater.* 398 (2010) 43.
- [18] S. Knitel, P. Spaetig, T. Yamamoto, H.P. Seifert, Y. Dai, G.R. Odette, *Nucl. Mater Energy*, 17 (2018) 69.
- [19] K. Wang, Y. Dai, P. Spatig, *J. Nucl. Mater.* 468 (2016) 246.
- [20] H. J. Jung, D. J. Edwards, R. J. Kurtz, G. R. Odette, Y. Wu, T. Yamamoto, DOE/ER-0313/58 (2015) 48-54.
- [21] L. Peng, Y. Dai, *J. Nucl. Mater.* 417 (2011) 996.
- [22] C. Vieh, "Hardening induced by radiation damage and Helium in structural materials," Ph. D Thesis, EPFL\_TH6490 (2015).
- [23] L. Peng, H. Ge, Y. Dai, Q. Huang, M. Ye, *J. Nucl. Mater.* 468 (2016) 255.
- [24] Yu.N. Osetsky and R.E. Stoller, *J. Nucl. Mater.* 465 (2015) 448.
- [25] M.E. Alam, T. Yamamoto, G.R. Odette, Engineering models for primary creep rates which mediate the high temperature dimensional stability of 9CrW tempered martensitic steel fusion structures, included in this DOE report DOE/ER-0313/68 (2020).
- [26] Y. Dai, G.R. Odette, T. Yamamoto, The Effects of Helium in Irradiated Structural Alloys. In: R.J.M. Konings and R.E. Stoller (eds.) *Comprehensive Nuclear Materials* 2<sup>nd</sup> edition, vol. 1, pp. 186–234. Oxford, Elsevier.